Sublimation from icy jets as a probe of the interstellar volatile content of comets

Geoffrey A. Blake[*][†], **C. Qi**[*], **Michiel R. Hogerheijde**[‡],
M. A. Gurwell[§] **& D. O. Muhleman**[*]

* *Division of Geological and Planetary Sciences, California Institute of Technology 150-21, Pasadena, California 91125, USA*
† *JILA, University of Colorado, Boulder, Colorado 80309, USA*
‡ *Department of Astronomy, University of California, Berkeley, California 94720, USA*
§ *Harvard-Smithsonian Center for Astrophysics, 60 Garden Street, Cambridge, Massachusetts 02138, USA*

Comets are some of the most primitive bodies left over from the Solar System's early history. They may preserve both interstellar material and material from the proto-solar nebula, and so studies of their volatile components can provide clues about the evolution of gases and ices, as a collapsing molecular cloud transforms into a mature planetary system[1,2]. Previous observations of emission from rotational transitions in molecules have averaged over large areas of the inner coma, and therefore include both molecules that sublimed from the nucleus and those that result from subsequent chemical processes in the coma. Here we present high-resolution observations of emission from the molecules HNC, DCN and HDO associated with comet Hale–Bopp. Our data reveal arc-like structures—icy jets—offset from (but close to) the nucleus. The measured abundance ratios on 1–3″ scales are substantially different from those on larger scales[3–5], and cannot be accounted for by models of chemical processes in the coma[2,6,7]; they are, however, similar to the values observed in the cores of dense interstellar clouds and young stellar objects. We therefore propose that sublimation from millimetre-sized icy grains ejected from the nucleus provides access to relatively unaltered volatiles. The D/H ratios inferred from our data suggest that, by mass, Hale–Bopp (and by inference the outer regions of the early solar nebula) consists of ≥15–40% of largely unprocessed interstellar material.

HNC is a metastable isomer of HCN, and is found in negligible amounts in equilibrium models of the solar nebula. Its detection in comets is thus an important indicator of kinetically controlled processes, that is, chemistry which is driven by the rates of various reactions and not by thermodynamics. Ion–molecule networks in dense molecular clouds[2,8,9] lead to HNC/HCN ratios of ≈0.2–1, while in analogues of the solar nebula, the T Tauri star accretion disks, values near 0.4 are seen[10]. In certain chemical kinetic models of these disks, the high HNC abundances are produced by photochemistry, while in others they arise from surviving molecular cloud material[11]. HNC can also be synthesized within the coma[6,7], and the radial dependence of the HNC/HCN ratio in comets should be a sensitive function of direct HNC outgassing versus *in situ* production[12].

D/H ratios can provide even more sensitive diagnostics of cometary origins. In dense clouds, trace species exhibit D/H enrichments of several orders of magnitude that are both molecule specific and temperature sensitive. The typical interstellar values are much larger than those expected for volatiles synthesized in proto-planetary regions of the solar nebula. For example, D/H ratios of 0.01–0.05 are common in molecular cloud organic compounds[13], while values of up to 0.18 have been detected towards low-mass protostars[9]. HDO/H_2O ratios are difficult to measure in cold regions, but lower bounds are provided by the values seen in hot cores[14] ($2-6 \times 10^{-4}$). These minimum HDO enhancements are still ten times the estimated protosolar deuterium fraction[15] of $(D/H)_{proto} \approx 3 \times 10^{-5}$, and are similar to the water D/H values

measured in comets Halley, Hyakutake and Hale–Bopp (3.1, 2.9, 3.3×10^{-4}) (refs 5, 16, 17). High-spatial-resolution studies of the molecular D/H variability should therefore provide clues as to the interstellar versus nebular contributions to cometary nuclei.

The HCN and HNC $1 \rightarrow 0$ transitions were observed simultaneously on 31 March 1997 with the Owens Valley Radio Observatory (OVRO) millimetre–array. Whereas the peak of the HCN emission is always found to lie within the width of a beam of the nucleus, weaker, more extended arcs are often observed whose position angles rotate with a period ($P_{nucleus}$) and phase that are
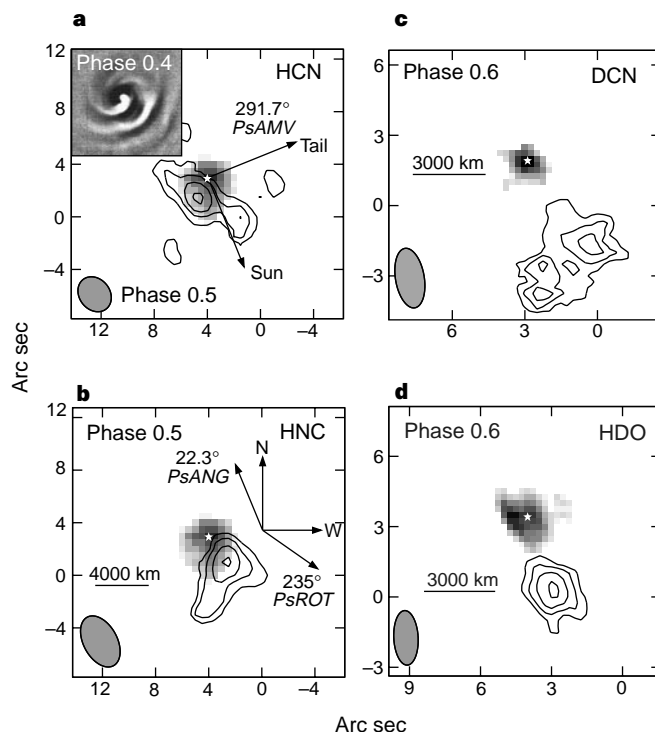
Figure 1 Contour images of millimetre-wave rotational line emission from the coma of comet Hale–Bopp. The full-width at half-maximum of the synthesized beam is shown by the ellipse in the lower left corner of each panel. Offsets (in arcsec) from the array pointing centre are indicated along the vertical and horizontal axes. Visibility phases and amplitudes were calibrated using interleaved observations of the quasar 0133+476, whereas measurements of Uranus, Neptune and the quasar 3C273 provided an absolute flux scale and determined the digital correlator passband. **a**, HCN $J = 1 \rightarrow 0$, $F = 2 \rightarrow 1$ (88.6318 GHz) emission. Contours start at 0.42 Jy beam^{-1} km s^{-1} and are spaced by 0.21 Jy beam^{-1} km s^{-1}. Arrows indicate the sky position angles (counter-clockwise from north) for the solar direction and the minus velocity vector (PsAMV) of the nucleus, while the upper left corner contains an optical image of the Hale–Bopp dust jets at a rotational phase of 0.4 on 2 April 1997 (ref. 19). **b**, HNC $1 \rightarrow 0$ (90.6635 GHz) emission. Contours start at 0.28 Jy beam^{-1} km s^{-1} and are spaced by 0.14 Jy beam^{-1} km s^{-1}. Arrows depict the cardinal directions, the position angle of the comet spin axis (N pole, PsROT), and the anti-solar direction (PsANG). Both **a** and **b** were measured between 31 March 1997 17:15 and 20:00 UT and integrated across the full velocity range (−1.3 to +1.3 km s^{-1}) in which emission is detected at the 2σ level. **c**, Velocity integrated (0–2.0 km s^{-1}) DCN $J = 3 \rightarrow 2$ (217.238 GHz) emission between 30 March 1997 17:30 and 22:30 UT. Contours start at 0.9 Jy beam^{-1} km s^{-1} and are spaced by 0.45 Jy beam^{-1} km s^{-1} **d**, Velocity integrated (−2.0 to 0 km s^{-1}) HDO $2_{11} \rightarrow 2_{12}$ (241.561 GHz) emission between 29 March 1997 19:30 and 30 March 00:30 UT. Contours start at 0.8 Jy beam^{-1} km s^{-1} and are spaced by 0.4 Jy beam^{-1} km s^{-1}. In each panel, the grey scale depicts the simultaneous observations of the dust and nucleus thermal continuum emission, the peak of which is marked by the star, while the definition of the rotational phase of the nucleus follows that of Licandro et al.[18]. The slight northeasterly shift of the nucleus position here and in Fig. 2 is due to uncertainties in the ephemeris used at the time of the observations.

well matched to that of the dust jets ($P_{nucleus} = 11.34 \pm 0.02$ h) (refs 18, 19). Analogous features are also observed in HNC. As Fig. 1a and b show, although extended HCN and HNC features are detected at position angles similar to those of the dust jets (position angle $\approx 230°$ in Fig. 1), over certain time ranges they are strongly anti-correlated in a radial sense.

We have calculated abundances towards the nucleus and at the jet positions using both local thermodynamic equilibrium (LTE, with a rotational temperature T_{ROT} of 115 K; ref. 3) and statistical equilibrium (SE) Monte Carlo codes (see Table 1). In the latter case, the molecular excitation is determined including both collisions and radiation, and a Monte Carlo approach is used to solve the line radiative transfer (ref. 20, and M.R.H. and F. van der Tak, manuscript in preparation) within a one-dimensional Hauser coma model at a total water production rate of 10^{31} mol s^{-1}. The model is sampled at the observational visibility plane, or (u, v), spacings, and the abundances are varied until agreement with the interferometric data is obtained. Accordingly, the effects of the varying spatial resolutions at wavelengths of $\lambda = 3.3$ and 1.4 mm and the finite array sampling of extended structures are rigorously accounted for. Densities in the inner coma are sufficiently high that departures from LTE are found to be quite small[3,5], while the SE models show that all of the transitions studied here are optically thin.

For HCN, the observed hyperfine ratios of the $1 \to 0$ transition are also consistent with low optical depths, as is true in larger beams[12]. Due to the large size of the coma and the coarse (u, v)–sampling of the present data sets, only 15–20% of the total flux within 45–60″ beams is detected. However, Hauser model fits with a single HCN production rate reproduce the OVRO $1 \to 0$, UMass 14 metre $1 \to 0$, and James Clerk Maxwell Telescope (JCMT) $4 \to 3$ intensities near perihelion[6,12], and demonstrate that the appropriate fluxes are recovered by the array even for sources which extend well beyond the primary beam of the six 10.4-m antennae. From images such as those in Fig. 1a we estimate that at most 20–25% of the total HCN $1 \to 0$ emission within 5″ of the nucleus arises in jet-like structures. When the extended coma emission and finite array (u, v)–sampling is accounted for, theoretically this fraction drops to ~15%.

For the other species, the observed anisotropy (Fig. 1b–d) renders spherically symmetric derivations of the production rates inappropriate. To account for this anisotropy, estimates of the jet solid-angle filling factors are needed. Here, the column densities in Table 1 have been scaled by the ratio of the jet/nucleus linewidths (≈ 0.5–0.6), an admittedly simplistic approach which should result in upper bounds to the jet production rates. The calculated HNC abundances are smaller than those observed by single dishes, and lend support to the idea that some HNC must be synthesized in the extended coma[6,7]. But the radial variation of a factor of 3 seen in the

HNC/HCN column-density ratios over a few thousand kilometres within the HNC arc are difficult to reconcile with the coma chemistry models[12].

Another illustration of the importance of jet activity comes from mapping the DCN and HDO emission. Figure 1c and d present images of DCN $3 \to 2$ and HDO $2_{11} \to 2_{12}$ transitions on 30 March and 29 March, respectively, at rotational phases (≈ 0.5–0.6) similar to those for HCN and HNC. DCN $3 \to 2$ images at two different rotational phases on 30 March are given in Fig. 2. The DCN and HDO position angles and the rotational sense of the DCN arcs are consistent with the known jetting properties of Hale–Bopp. Although we do not have simultaneous HCN and DCN observations, the HCN column densities on 31 March are in excellent agreement with UMass $1 \to 0$ single-dish maps on 30 March (A. J. Lowell, personal communications). Using the 31 March HCN fluxes at similar rotational phases, the DCN/HCN production-rate ratios in the icy jets vary by factors of at least two but are always quite large, $(D/H)_{HCN,jet} \lesssim 0.025$, compared with the value of 2.3×10^{-3} found by JCMT observations of the DCN $5 \to 4$ transition[4]. Ratios with the 29 March HCN data are even larger, as are the direct ratios of the observed column densities.

Absorption by atmospheric water vapour makes direct measurements of the HDO/H_2O ratio impractical, but the OVRO fluxes and the large-scale water outgassing (from centimetre measurements of OH; ref. 3) of 10^{31} s^{-1} yield a lower bound of $(D/H)_{H_2O,jet} \gtrsim 7.5 \times 10^{-4}$. To estimate the jet D/H ratios we use the simultaneously observed HCN emission as a proxy. Provided the HCN/H_2O ratio in the jets is similar to the value of 0.002 observed in single-dish beams[3,21], the interferometric HDO/HCN production rates translate into a $(D/H)_{H_2O,jet}$ estimate of 1.5–2.5×10^{-3}. This latter value is again nearly an order of magnitude larger than that found in the 10.5″ beam of the JCMT[5], and over 20 times the D/H ratio of the Earth's oceans.

What processes could cause such significant differences between the volatile ratios on single-dish and interferometric scales? It is now clear that grains that are larger than about 1 mm are lifted by jet activity[21,22]. Once exposed to the Sun, these grains warm rapidly and any volatiles are released. Single-dish examinations of Hale–Bopp average over distances of at least 8,000–10,000 km, whereas the resolution and spatial filtering of the array enables the emission associated with the dust/gas jets close to the nucleus to be selectively highlighted.

Gases subliming from the nucleus must pass through warm surface layers, while those released from grains in the coma pass through less material but are exposed to intense solar radiation. Studies of crystalline ice in the 140–210 K range have shown that a viscous water layer coexists ubiquitously[23]. Little is at present known about the stability of HNC against isomerization to HCN as it diffuses through warm ice, water, and dust, but the rapid radial

Table 1 Observations and abundance ratios

Date	Species, location	I (K km s^{-1})	N_{LTE} (10^{13} mol cm^2)	Q_{LTE} (10^{26} mol s^{-1})	Q_{SE} (10^{26} mol s^{-1})	R_{LTE}	R_{SE}
29/03/97	HCN, nuc.	13.1	2.8	66	130	NA	NA
29/03/97	HCN, jet	8.5	18	42	57	NA	NA
29/03/97	HDO, nuc.	<3.0	<52	<140	<150	<1.2	<0.8
29/03/97	HDO, jet	10.7	170	150	240	1.6	2.2
30/03/97	DCN, nuc.	<2.5	<0.6	<0.7	<1.7	<0.006	<0.008
30/03/97	DCN, jet	11.5–14.4	2.7–3.4	1.9–2.2	3–4	≤ 0.024	≤ 0.036
31/03/97	HCN, nuc.	20.8	44	120	200	NA	NA
31/03/97	HCN, jet	15.9	34	92	110	NA	NA
31/03/97	HNC, nuc.	3.8	5.2	14	15	0.12	0.08
31/03/97	HNC, jet	11.7	16	22	23	0.24	0.21

Integrated intensities (I) are shown for the $J = 1 \to 0$ transitions of HCN (specifically, the $F = 2 \to 1$ component) and HNC, the $J = 3 \to 2$ transition of DCN, and the $2_{11} \to 2_{12}$ transition of HDO. Thermal equilibrium column densities (N_{LTE}) are reported, as are spherically symmetric production rates calculated with either a local thermodynamic equilibrium (Q_{LTE}) or statistical equilibrium (Q_{SE}) Hauser model. For collisional rates in the SE model, the 'interstellar' cross-sections for collisions with H_2 molecules[27] are scaled to reproduce the total 'cometary' cross-sections recommended by Crovisier[28] and Meier *et al.*[4]. Use of the H_2 cross-sections themselves (which are roughly an order of magnitude smaller) only changes the production rates by less than 10% as the levels observed are nearly in LTE. Abundance ratios with respect to HCN (R_{LTE}, R_{SE}) are calculated using the production rates derived from the LTE and Monte Carlo models. To account for the jet anisotropy, production rates at positions offset from the nucleus have been calculated according to $Q_{jet}(X) = Q_{Hauser} \times \Delta v_X / \Delta v_{nucleus}$, where Δv_X is the measured velocity width of species X at the jet position, and $\Delta v_{nucleus}$ is the measured velocity width of HCN emission at the nucleus. NA, not applicable.

variability of the HNC/HCN ratio suggests that some alteration occurs. Further, the acidity of HCN is sufficient to exchange D/H even in layers of water only a few micrometres thick under laboratory conditions. The D/H ratio of HCN, and by inference the D/H ratio of other trace species with labile hydrogens (NH_3, CH_3OH, HCOOH, and so on), subliming from the nucleus of comets may therefore be controlled by that of the main constituent, water.
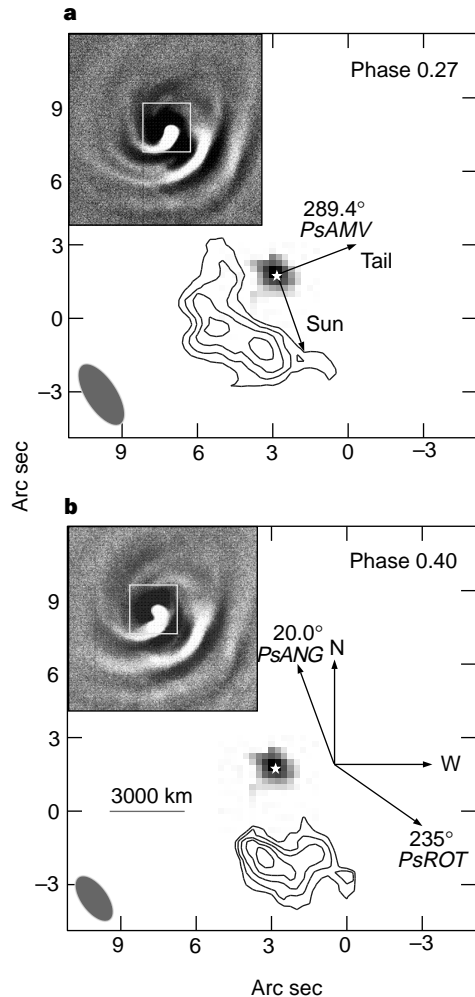
Figure 2 OVRO images of the DCN $J = 3 \rightarrow 2$ (217.238 GHz) emission in the coma of Hale–Bopp. Ellipses denote the full-width at half-maximum of the synthesized beam ($\approx 2.9'' \times 1.3''$), while the grey scale depicts the simultaneously measured dust continuum emission, the peak of which is denoted in the main panels by the star. Offsets from the array pointing centre are given in arc seconds. **a**, Velocity-integrated (-2.0 to $0 \, km \, s^{-1}$) DCN emission between 30 March 1997 15:40 and 18:30 UT. The contours start at $0.66 \, Jy \, beam^{-1} \, km \, s^{-1}$ and are spaced by $0.33 \, Jy \, beam^{-1} \, km \, s^{-1}$. Arrows indicate the position angles of the solar direction and the minus velocity vector (PsAMV) of the comet. Inset, an optical image of dust jets in the coma of Hale–Bopp taken on 1 April 1997 at a rotational phase of 0.26 (ref. 19), with the box depicting the area shown in the OVRO image. **b**, Velocity-integrated (-2.0 to $0 \, km \, s^{-1}$) DCN emission between 30 March 1997 16:30 and 20:30 UT. Contours start at $0.44 \, Jy \, beam^{-1} \, km \, s^{-1}$ and are spaced by $0.22 \, Jy \, beam^{-1} \, km \, s^{-1}$. Arrows depict the cardinal directions, the position angle of the comet's north pole (PsROT), and the anti-solar direction (PsANG). The inset shows a dust-jet optical image, taken on 2 April 1997 at a rotational phase of 0.4. For all the optical images, computer processing has been used to enhance the contrast and highlight the structure in the gas/dust distributions. While the DCN emission is entirely displaced from the nucleus, simultaneous observations of the $H_2S \, 2_{20} \rightarrow 2_{11}$ transition at 216.7104 GHz reveal intense emission centred on the dust continuum.

If such an exchange process occurs, those $(D/H)_{HCN}$ ratios smaller than 0.025 that are measured in the DCN arcs may be more representative of the ices trapped within the nucleus; ices that would otherwise be detectable only with direct sampling techniques. As the region of high D/H gas is small and mixed with sublimation from the nucleus itself, it is difficult to detect in larger beams, suggesting that the D/H ratios in trace species with exchangeable hydrogen atoms should be viewed with caution when averaged over large spatial dimensions. To be consistent with the JCMT DCN/HCN ratio, the DCN jets can represent at most 10–15% of the total gas production rate. This is somewhat larger than the mass-loss rate of millimetre-sized grains from Hyakutake[22], but is consistent with the HCN limits noted above.

Such large, differential D/H fractionations are difficult to produce under the conditions of high temperature and pressure found near jovian protoplanetary sub-nebulae[2]. They are, however, entirely consistent with those seen in dense cloud cores at $\sim 20–30 \, K$. High, variable D/H ratios may also prevail in the outermost regions of the solar nebula where the chemical kinetic timescales can greatly exceed the dynamical lifetimes[2]. Similar formation temperatures for individual species have been deduced for Hale–Bopp from measurements of the *ortho-para* ratio in water[24], and are consistent with the tentative detection of Ar at cosmogonic values[25].

Further estimates of the degree of mixing of protoplanetary and presolar material can be constrained by the observed HDO/H_2O ratios. If the protosolar deuterium fraction[15] is assumed to represent the (warm) nebular end member, a mass-balance calculation using the OVRO HDO/H_2O upper and lower limits and the single-dish HDO measurements yields interstellar mass fractions of at least 15% and 40%. Higher nebular D/H values lower the instellar fraction, but would themselves be evidence of inherited material.

The high D/H ratios of the Hale–Bopp jets are therefore most simply explained by the survival of substantial reservoirs of presolar volatiles that did not equilibrate with the surrounding nebular gas. We stress that this does not imply that comets must contain assemblages of pristine interstellar ices[2,4]. Sublimation of interstellar grain mantles as they pass through the nebular accretion shock is likely to occur, for example, as is radial mixing. Subsequent recondensation and grain growth is rapid, and the 50–70 K temperatures inferred from the abundances of volatiles such as CO, CH_4 and C_2H_6 are likely to measure the physical conditions under which the bulk of the nucleus was assembled[26], and need not be identical to molecular D/H or nuclear spin temperatures, which can be set at earlier times. □

1. Festou, M. C., Rickman, H. & West, R. M. Comets. II. Models, evolution, origin, and outlook. *Astron. Astrophys. Rev.* **5**, 37–163 (1993).
2. Irvine, W. M., Schloerb, F., Crovisier, J., Fegley, B. & Mumma, M. in *Protostars & Planets IV* (eds Mannings, V., Boss, A. & Russell, S.) (Univ. Arizona Press, Tucson, in the press).
3. Biver, N. et al. Evolution of the outgassing of comet Hale-Bopp (C/1995 O1) from radio observations. *Science* **275**, 1915–1918 (1997).
4. Meier, R. et al. Deuterium in comet C/1995 O1 (Hale-Bopp): Detection of DCN. *Science* **279**, 1707–1710 (1998).
5. Meier, R. et al. A determination of the HDO/H₂O ratio in comet C/1995 O1 (Hale-Bopp). *Science* **279**, 842–844 (1998).
6. Irvine, W. M. et al. Chemical processing in the coma as the source of cometary HNC. *Nature* **393**, 547–550 (1998).
7. Rodgers, S. & Charnley, S. HNC & HCN in comets. *Astrophys. J.* **501**, L227–250 (1998).
8. Schilke, P. et al. A study of HCN, HNC, and their isotopomers in OMC-1. *Astron. Astrophys.* **256**, 595–612 (1992).
9. Van Dishoeck, E. F., Blake, G. A., Jansen, D. J. & Groesbeck, T. D. Molecular abundances and low mass star formation. II. Organic and deuterated species toward IRAS 16293-2422. *Astrophys. J.* **447**, 760–782 (1995).
10. Dutrey, A., Guilloteau, S. & Guelin, M. Chemistry of protosolar-like nebulae: The molecular content of the DM Tau and GG Tau disks. *Astron. Astrophys.* **317**, L55–58 (1997).
11. Willacy, K., Klahr, H. H., Millar, T. J. & Henning, T. Gas and grain chemistry in a protoplanetary disk. *Astron. Astrophys.* **338**, 995–1006 (1998).
12. Irvine, W. M. et al. Chemistry in cometary comae. *Faraday Discuss.* **109**, 475–492 (1998).
13. Wootten, A. in *Astrochemsitry* (eds Vardya, M. S. & Tarafdar, S. P.) 311–319 (IAU Symp. 120, Reidel, Dordrecht, 1987).
14. Jacq, T. et al. Deuterated water and ammonia in hot cores. *Astron. Astrophys.* **228**, 447–470 (1990).
15. Gautier, D. & Morel, P. A reestimate of the protosolar (D/H)ₚ ratio from (³He/⁴He)ₛw solar wind measurements. *Astron. Astrophys.* **323**, L9–L12 (1997).
16. Eberhardt, P., Reber, M., Krankowsky, D. & Hodges, R. R. The D/H and ¹⁸O/¹⁶O ratios in water from comet P/Halley. *Astron. Astrophys.* **302**, 301–316 (1995).

17. Bockelée-Morvan, D. *et al.* Deuterated water in comet C/1996 B2 (Hyakutake) and its implications for the origin of comets. *Icarus* **133**, 147–162 (1998).

18. Licandro, J. *et al.* The rotation period of C/1995 O1 (Hale-Bopp). *Astrophys. J.* **501**, L221–L225 (1998).

19. Mueller, B. E. A., Samarasinha, N. H. & Belton, M. J. S. Imaging of the structure and evolution of the coma morphology of Comet Hale-Bopp (C/1995 O1). *Earth, Moon, Planets* (in the press).

20. Hogerheijde, M. R. The molecular environment of low-mass protostars. Thesis, Leiden Univ. (1998).

21. Bockelée-Morvan, D. & Rickman, H. C/1995 O1 (Hale-Bopp): Gas production curves and their interpretation. *Earth, Moon, Planets* (in the press).

22. Harmon, J. K. *et al.* Radar detection of the nucleus and coma of comet Hyakutake (C/1996 B2). *Science* **278**, 1921–1924 (1997).

23. Jenniskens, P., Banham, S. F., Blake, D. F. & McCoustra, M. R. S. Liquid water in the domain of cubic crystalline ice I$_c$. *J. Chem. Phys.* **107**, 1232–1241 (1997).

24. Crovisier, J. *et al.* The spectrum of comet Hale-Bopp (C/1995 O1) observed with the Infrared Space Observatory at 2.9 AU from the Sun. *Science* **275**, 1904–1907 (1997).

25. Stern, A., Slater, D. C., Festou, M. C., Parker, J. W. & A'Hearn, M. F. The EUV spectrum and the discovery of argon in Hale-Bopp. *Science* (submitted).

26. Notesco, G., Laufer, D. & Bar-Nun, A. The source of the high C_2H_6/CH_4 ratio in comet Hyakutake. *Icarus* **125**, 471–473 (1997).

27. Green, S., McLean, S. & McLean, A. D. Improved collisional excitation rates for interstellar water. *Astrophys. J. Suppl. Ser.* **85**, 181–185 (1993).

28. Crovisier, J. Rotational and vibrational synthetic spectra of linear parent molecules in comets. *Astron. Astrophys. Suppl. Ser.* **68**, 223–258 (1987).

Gravity-wave interferometers as quantum-gravity detectors

Giovanni Amelino-Camelia*

Institut de Physique, Université de Neuchâtel, CH-2000 Neuchâtel, Switzerland

Nearly all theoretical approaches to the unification of quantum mechanics and gravity predict[1–4] that, at very short distance scales, the classical picture of space-time breaks down, with space-time becoming somewhat 'fuzzy' (or 'foamy'). The properties of this fuzziness and the length scale that characterizes its onset are potentially a means for determining which (if any) of the existing models of quantum gravity is correct. But it is generally believed[5] that these quantum space-time effects are too small to be probed by technologies currently available. Here I argue that modern gravity-wave interferometers are sensitive enough to test certain space-time fuzziness models, because quantum space-time effects should provide an additional source of noise in the interferometers that can be tightly constrained experimentally. The noise levels recently achieved in one interferometer[6] are sufficient to rule out values of the length scale that characterizes one of the space-time fuzziness models down to the Planck length ($\sim 10^{-35}$ m) and beyond, while the sensitivity required to test another model should be achievable with interferometers now under construction.

In a fuzzy space-time, the operative definition of a distance D is affected by quantum fluctuations. These fluctuations are primarily characterized by their overall magnitude σ_D (the root-mean-square deviation of D). The simplest proposals are such that:

$$\sigma_D \gtrsim L_{\min} \qquad (1)$$

where $L_{\min}$ is a quantum-gravity scale expected to be simply related to (usually identified with) the Planck length. Relations of the type shown in equation (1) are motivated by certain analyses of *gedanken* experiments (see, for example, ref. 7) that combine some elements of quantum mechanics and some elements of gravity. The quantum space-time fluctuations responsible for equation (1) are often

visualized as involving geometry and topology fluctuations[1], virtual black holes[4] and other unusual phenomena.

Other models for space-time fuzziness arise when taking into account the quantum properties of devices, which were ignored in the original studies[7] that led to the proposal of equation (1). It is well understood (see, for example, refs 8–13) that the combination of the gravitational properties and the quantum properties of devices can be important in the analysis of the operative definition of gravitational observables. The implications can be far-reaching; in particular, it was observed[11] that the masses of the probes used in measurements induce a change in the space-time metric, and this is associated with the emergence of non-locality. The nature of the gravitationally induced non-locality suggests[11] a modification of the fundamental commutators.

Here I shall be primarily concerned with the role that the quantum and the gravitational properties of devices have in the analysis of the measurability of distances, in the sense first illustrated by Wigner[14]. Wigner derived a quantum limit on the measurability of the distance D separating two bodies by analysing a measurement procedure based on the exchange of a light signal between the bodies. Taking into account Heisenberg's position–momentum uncertainty relations for the clock used in the measurement procedure, Wigner obtained a lower bound on the quantum uncertainty in D:

$$\delta D \geq \sqrt{\frac{\hbar T_{\mathrm{obs}}}{2 M_c}} \approx \sqrt{\frac{\hbar D}{c M_c}} \qquad (2)$$

where M_c is the mass of the clock, T_{obs} is the time required by the measurement procedure, and on the right-hand side I use the fact that the Wigner measurement of a distance D requires a time $2D/c$, where c is the speed of light.

The result shown in equation (2) may at first appear puzzling, as ordinary quantum mechanics should not limit the measurability of any given observable. (It only limits the combined measurability of pairs of conjugate observables.) However, quantum mechanics is the theoretical framework for the description of the outcome of experiments performed by classical devices. In the limit in which the devices (for example, Wigner's clock) behave 'classically', which in particular requires the devices to be infinitely massive (so that $\delta x \delta v \approx \hbar/m \approx 0$), the right-hand side of equation (2) tends to zero. (Here δx and δv denote, respectively, the quantum uncertainties in the position and in the velocity of the device.) Therefore, as expected, there is no limitation on the measurability of the distance D in the appropriate infinite-mass 'classical-device limit'. This line of argument depends crucially on the fact that ordinary quantum mechanics does not involve gravity.

The classical infinite-mass limit is clearly not consistent with the nature of measurements involving gravitational effects. As the devices get more and more massive they increasingly disturb the gravitational/geometrical observables, and well before reaching the infinite-mass limit the procedures for the measurement of gravitational observables cannot be meaningfully performed[10,12,13]. A well-known example of this problem has been encountered in attempts (see, for example, ref. 8) to generalize to the study of the measurability of gravitational fields the Bohr–Rosenfeld analysis[15] of the measurability of the electromagnetic field. To achieve the accuracy allowed by the formalism of ordinary quantum mechanics, the Bohr–Rosenfeld measurement procedure resorts to ideal test particles of infinite mass, which would of course not be admissible probes in a gravitational context. Similarly, in Wigner's measurement procedure, the limit $M_c \rightarrow$ infinity is not admissible when gravitational interactions are taken into account. At the very least, the value of M_c is limited by the requirement that the clock should not turn into a black hole (which would not allow the required exchange of signals between the clock and the other devices). These observations, which render unavoidable the dependence on T_{obs} of equation (2), provide a basis for the possibility[12,13] that in quantum